

Iterative Reconstruction of the Electron Density and Effective Atomic Number using a Non-Linear Forward Model

K. Aditya Mohan^a, Kyle M. Champley^a, Albert W. Reed^b, Steven M. Glenn^a, and Harry E. Martz Jr.^a

^aLawrence Livermore National Laboratory, Livermore, CA, USA

^bArizona State University, Tempe, AZ, USA

ABSTRACT

For material identification, characterization, and quantification, it is useful to estimate system-independent material properties that do not depend on the detailed specifications of the X-ray computed tomography (CT) system such as spectral response. System independent ρ_e and Z_e (SIRZ) refers to a suite of methods for estimating the system independent material properties of electron density (ρ_e) and effective atomic number (Z_e) of an object scanned using dual-energy X-ray CT (DECT). The current state-of-the-art approach, SIRZ-2, makes certain approximations that lead to inaccurate estimates for large atomic numbered (Z_e) materials. In this paper, we present an extension, SIRZ-3, which iteratively reconstructs the unknown ρ_e and Z_e while avoiding the limiting approximations made by SIRZ-2. Unlike SIRZ-2, this allows SIRZ-3 to accurately reconstruct ρ_e and Z_e even at large Z_e . SIRZ-3 relies on the use of a new non-linear differentiable forward measurement model that expresses the DECT measurement data as a direct analytical function of ρ_e and Z_e . Leveraging this new forward model, we use an iterative optimization algorithm to reconstruct (or solve for) ρ_e and Z_e directly from the DECT data. Compared to SIRZ-2, we show that the magnitude of performance improvement using SIRZ-3 increases with increasing values for Z_e .

Keywords: DECT, dual-energy, SIRZ, rho-e, Z-e, system independent features, electron density, effective atomic number, reconstruction, X-ray, forward model, optimization. .

1. INTRODUCTION

X-ray computed tomography (CT) is widely used to reconstruct the spatially varying linear attenuation coefficient (LAC) of an object.¹ The spectral response function that is dependent on the X-ray source and the detector is used to quantify the variation in X-ray intensity over the broad range of emitted X-ray energies. Most CT systems have differing spectral response functions that causes the reconstructed LAC to be dependent on the spectral response of the X-ray scanner. Hence, it is not possible to compare the LAC values reconstructed using different X-ray scanners. Also, the estimated LAC does not provide direct information on the density and atomic composition of an object.²

Dual-energy X-ray computed tomography (DECT) is useful to estimate system independent properties that are independent of the CT system spectral response and other system specifications. Our laboratory based micron scale DECT system scans the same object twice using two different spectra. Using DECT scans, an approach called SIRZ was proposed³ to estimate the system independent properties of electron density, ρ_e , and effective atomic number, Z_e . The electron density, ρ_e , is a direct measure of the object's density and the effective atomic number, Z_e , is useful to predict the atomic composition. In Champley at al.,² the authors presented the SIRZ-2 approach that improved upon the original SIRZ to produce more accurate estimates for ρ_e and Z_e . SIRZ-2 can be broadly split into four different steps:

1. Preprocessing steps that include detector gain correction, detector deblur, and scatter correction.

Further author information: (Send correspondence to K. A. M.)

K. A. M.: E-mail: mohan3@llnl.gov; K. M. C.: E-mail: champley1@llnl.gov; A. W. R.: E-mail: awreed@asu.edu; S. M. G.: E-mail: glenn21@llnl.gov; H. E. M.: E-mail: martz2@llnl.gov.

2. Dual-energy basis decomposition to estimate projections of the object at two different synthesized monochromatic basis (SMB) energies.
3. Filtered back-projection to reconstruct the LAC values at the two SMB energies,
4. Estimation of electron density and effective atomic number from the LACs at the two SMB energies.

The second and fourth steps of SIRZ-2 are based on simplifying approximations that limit its accuracy.

In this paper, we present a new approach called SIRZ-3 to reconstruct the system independent properties of ρ_e and Z_e while avoiding the approximations made in SIRZ-2. SIRZ-3 replaces the steps 2, 3, and 4 of SIRZ-2 using a single iterative optimization algorithm. Features of the SIRZ-3 method include:

- Non-linear differentiable forward model that expresses the measured DECT data as a direct function of the object's spatial distribution of ρ_e and Z_e .
- Formulation of an error function that quantifies the deviation of measured data from the output of the forward model given the unknowns, (ρ_e, Z_e) .
- Method for reconstructing (ρ_e, Z_e) from the measured data by minimizing the error function using the limited memory Broyden–Fletcher–Goldfarb–Shanno (L-BFGS) solver.^{4,5}

2. BACKGROUND

The LAC quantifies the magnitude of X-ray attenuation within an object. The LAC varies as a function of the position inside the object, density, atomic composition, and X-ray energy. The dependence of LAC, denoted as $\mu(Z, \rho_e, E)$, on the electron density, ρ_e , and atomic number, Z , is given by,

$$\mu(Z, \rho_e, E) = \rho_e \sigma_e(Z, E), \quad (1)$$

where E is the X-ray energy, $\sigma_e(\cdot)$ is the total X-ray electronic cross-section.² Equation (1) is only defined for integer valued Z that correspond to pure elements.

In order to represent compounds or mixtures of elements, the cross-section for non-integer Z_e is defined as follows,³

$$\sigma_e(Z_e, E) = (1 - \delta) \sigma_e(Z', E) + \delta \sigma_e(Z' + 1, E), \quad (2)$$

where $Z' = \lfloor Z_e \rfloor$, and $\delta = (Z_e - Z')$. Note that Z_e for a given compound or mixture is not a fundamental physical constant and there are several competing techniques to define Z_e . We adopt the definition of Z_e from Champley et al.² since it is a function of the X-ray cross-section with superior system invariance properties. The Z_e for a compound or mixture is defined as,

$$Z_e = \arg \min_z \left\{ \int_E S(E) [\exp(-M\sigma_e(z, E)) - \exp(-M\sigma_c(E))]^2 dE \right\}, \quad (3)$$

where $\sigma_c(E)$ is the tabulated⁶ electron cross-section of the material, $S(E)$ is the spectral response at energy E , and M is the areal electron density. This definition in (3) is demonstrated to be relatively insensitive to $S(E)$ and the X-ray energy range of interest (30-200keV). For additional details on the definition of Z_e and its estimation, the reader may refer to Champley et al.⁷

3. FORWARD MODEL

In this section, we formulate a forward model that mathematically expresses the measured DECT data as a function of the object properties, ρ_e and Z_e . This forward model is necessary to solve the inverse problem of reconstructing the object's ρ_e and Z_e .

The forward model is derived in discrete coordinate space. Let $\rho_{e,j}$ and $Z_{e,j}$ represent the ρ_e and Z_e values respectively at the j^{th} voxel inside the object. Then, the LAC at voxel j is given by $\mu_{j,k} = \rho_{e,j}\sigma_k(Z_{e,j})$, where $\sigma_k(Z_{e,j}) = \sigma_e(Z_{e,j}, E_k)$ from (2) and E_k is the X-ray energy at the k^{th} energy bin. The linear projections (line-integration) of the LAC is expressed as,

$$p_{i,k} = \sum_j A_{i,j} \mu_{j,k}, \quad (4)$$

where $A_{i,j}$ is the element along the i^{th} row and j^{th} column of the matrix A . At the detector, the measurement is the average transmission function $\exp(-p_{i,k})$ weighted by the spectral density function S_k . Hence, the effective transmission is given by,

$$t_i = \sum_k S_k \exp(-p_{i,k}), \quad (5)$$

where S_k is the spectral density at the k^{th} energy bin (S_k is a discretized version of $S(E)$ used in (3)) such that $\sum_k S_k = 1$. The spectral density function S_k quantifies both the spectral density of the X-ray source and the spectral response of the detection system. We compute the negative logarithm of (5), which gives us the measurement data in attenuation space, $-\log(t_i)$.

For DECT, the complete forward model is,

$$\tilde{y}_i^L = -\log \left(\sum_k S_k^L \exp \left\{ -\sum_j A_{i,j} \rho_{e,j} \sigma_k(Z_{e,j}) \right\} \right), \quad (6)$$

$$\tilde{y}_i^H = -\log \left(\sum_k S_k^H \exp \left\{ -\sum_j A_{i,j} \rho_{e,j} \sigma_k(Z_{e,j}) \right\} \right), \quad (7)$$

where S_k^L is the spectral density for X-rays at the low-energy spectrum, S_k^H is the spectral density at the high-energy spectrum, and \tilde{y}_i^L and \tilde{y}_i^H are the forward model predictions for the low-energy and high-energy measurements respectively. To ensure differentiability of the forward model in (6) and (7), we need analytical derivatives for $\sigma_k(Z_{e,j})$ with respect to $Z_{e,j}$. This derivative is given by,

$$\frac{\partial \sigma_k(Z_{e,j})}{\partial Z_{e,j}} = \sigma_k(Z'_{e,j} + 1) - \sigma_k(Z'_{e,j}), \quad (8)$$

where $Z'_{e,j} = \lfloor Z_{e,j} \rfloor$ and $\lfloor \cdot \rfloor$ is the floor function.

4. SIRZ-3: RECONSTRUCTION BY OPTIMIZATION

SIRZ-3 is a framework to solve the problem of reconstructing $\rho_{e,j}$ and $Z_{e,j}$ from measurements y_i^L and y_i^H using a forward model that accurately defines an analytical relation between (y_i^L, y_i^H) and $(\rho_{e,j}, Z_{e,j})$ for all i and j . SIRZ-3 adopts an iterative approach, where the solution for $(\rho_{e,j}, Z_{e,j})$ is iteratively refined such that the output of the forward model (whose input is the current estimate for $\rho_{e,j}$ and $Z_{e,j}$) gets progressively closer to the measurements (y_i^L, y_i^H) . In addition to a forward model, the solution for $(\rho_{e,j}, Z_{e,j})$ may also be required to satisfy certain sparsity enforcing regularization criteria using a prior model. In this paper, however, we do not use a prior model.

The analytical relation for the forward model used in this paper is shown in equations (6) and (7). The accuracy of SIRZ-3 is dependent on the accuracy of this analytical relation that mathematically describes the measurement process of our X-ray system. Future efforts to improve SIRZ-3 may potentially focus on more

accurate forward models that improve upon equations (6) and (7) or more accurate preprocessing algorithms so that (6) and (7) does accurately model the data.

To formulate the reconstruction algorithm, we define the following error function,

$$E(y^L, y^H; \rho_e, Z_e) = \sum_i w_i^L (y_i^L - \tilde{y}_i^L)^2 + \sum_i w_i^H (y_i^H - \tilde{y}_i^H)^2, \quad (9)$$

where y_i^L and y_i^H are the attenuation space measurements at the low-energy and high-energy spectra respectively, and \tilde{y}_i^L and \tilde{y}_i^H are the forward model predictions from (6) and (7) respectively. The weights for the penalty terms are given by $w_i^L = \exp(-y_i^L)/N$ and $w_i^H = \exp(-y_i^H)/N$, where N is the number of sinogram pixels summed over all the views. Substituting (6) and (7) in (9), we get,

$$E(y^L, y^H; \rho_e, Z_e) = \sum_i w_i^L \left(y_i^L + \log \left[\sum_k S_k^L \exp \left\{ - \sum_j A_{i,j} \rho_{e,j} \sigma_k(Z_{e,j}) \right\} \right] \right)^2 + \sum_i w_i^H \left(y_i^H + \log \left[\sum_k S_k^H \exp \left\{ - \sum_j A_{i,j} \rho_{e,j} \sigma_k(Z_{e,j}) \right\} \right] \right)^2, \quad (10)$$

where Z_e is a vector of all $Z_{e,j}$ voxel values, ρ_e is a vector of all $\rho_{e,j}$ voxel values. Note that the projection matrix entries $A_{i,j}$ are stored in a memory-efficient sparse representation that only stores the non-zero values and its locations. We used LTT⁷ to generate $A_{i,j}$. Then, the reconstruction of SIRZ-3 is obtained by solving,

$$\left(\hat{\rho}_e, \hat{Z}_e \right) = \arg \min_{\rho_e, Z_e} E(y^L, y^H; \rho_e, Z_e), \text{ s.t. } \rho_e^{\min} \leq \rho_{e,j} \leq \rho_e^{\max} \text{ and } Z_e^{\min} \leq Z_{e,j} \leq Z_e^{\max}, \quad (11)$$

where \hat{Z}_e and $\hat{\rho}_e$ are reconstructions of Z_e and ρ_e respectively, ρ_e^{\min} and ρ_e^{\max} are the lower and upper limits for $\rho_{e,j}$ respectively, and Z_e^{\min} and Z_e^{\max} are the lower and upper limits for $Z_{e,j}$ respectively. In this paper, we set $Z_e^{\min} = 1$, $Z_e^{\max} = 118$, $\rho_e^{\min} = 0$, and $\rho_e^{\max} = 9.018507 \times 10^{-3}$ electrons \times mol/mm³.

In order to improve conditioning and ensure fast convergence, we optimize z-score normalized versions of Z_e and ρ_e . Let Z_e^{avg} and Z_e^{std} be the mean and standard deviation of the SIRZ-2 reconstructed voxel values for Z_e . Similarly, let ρ_e^{avg} and ρ_e^{std} be the mean and standard deviation of the SIRZ-2 reconstructed voxel values for ρ_e . Then, we solve,

$$\left(\hat{\rho}_e^{nm}, \hat{Z}_e^{nm} \right) = \arg \min_{\rho_e^{nm}, Z_e^{nm}} E(y^L, y^H; \rho_e^{std} \rho_e^{nm} + \rho_e^{avg}, Z_e^{std} Z_e^{nm} + Z_e^{avg}), \text{ s.t. } \rho_e^{\min} \leq \rho_e^{std} \rho_{e,j}^{nm} + \rho_e^{avg} \leq \rho_e^{\max} \text{ and } Z_e^{\min} \leq Z_e^{std} Z_{e,j}^{nm} + Z_e^{avg} \leq Z_e^{\max}, \quad (12)$$

where we use vector-scalar multiplication^{*} and vector-scalar addition[†] within the error function $E(\cdot)$. The SIRZ-3 reconstruction is given by,

$$\hat{Z}_e = Z_e^{std} \hat{Z}_e^{nm} + Z_e^{avg} \text{ and } \hat{\rho}_e = \rho_e^{std} \hat{\rho}_e^{nm} + \rho_e^{avg}. \quad (13)$$

We use the python programming language and pytorch framework for implementing and solving (12). Pytorch's algorithmic differentiation is used to compute the partial derivatives of $E(\cdot)$ with respect to $Z_{e,j}^{nm}$ and $\rho_{e,j}^{nm}$. We solve equation (12) using the L-BFGS^{4,5} optimization algorithm. Upon convergence and using (13), L-BFGS yields the reconstruction of the electron density, $\hat{\rho}_e$, and the effective atomic number, \hat{Z}_e . We use the LBFGS implementation by Shi et al.⁸ For LBFGS, we use a history size of 64, weak Wolfe line search, and a convergence criteria that stops the LBFGS iterations when the percentage change in both Z_e and ρ_e goes below 0.2% for 10 consecutive iterations. Note that it is important to have a sufficiently strong convergence criteria along with sufficiently large history size to ensure convergence. We use the SIRZ-2 estimates for Z_e and ρ_e to initialize the optimization in (12).

^{*}Vector-scalar multiplication is point wise multiplication of a scalar to every element of a vector.

[†]Vector-scalar addition is point wise addition of a scalar to every element of a vector.

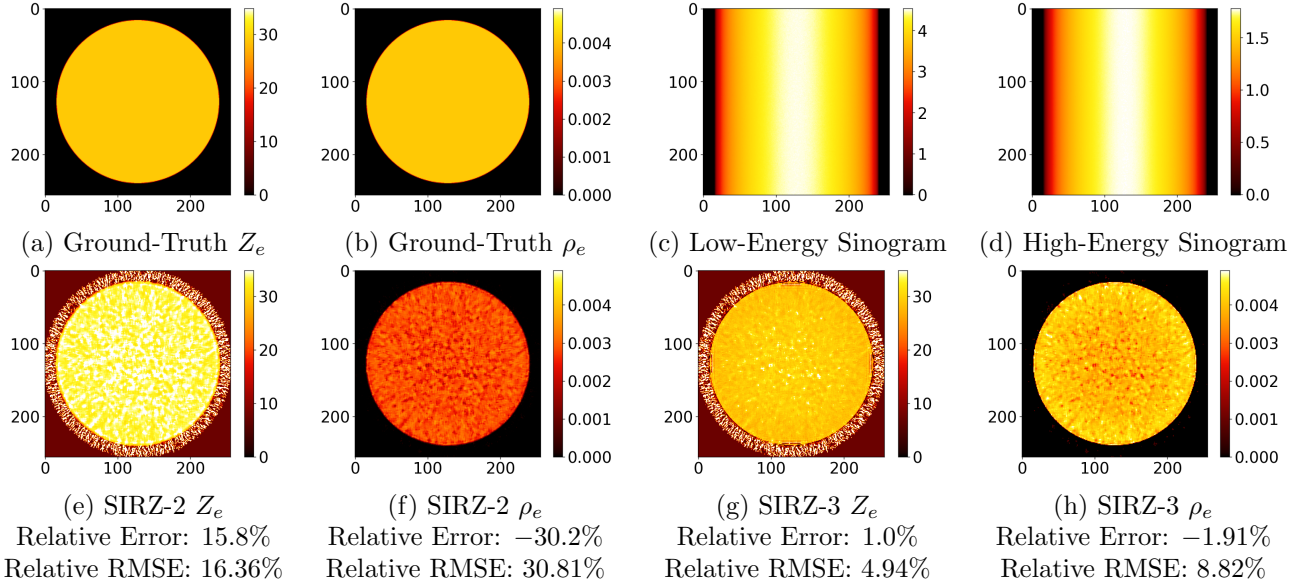


Figure 1. (Z_e, ρ_e) reconstruction of a 4mm diameter copper (Cu) disc with a maximum attenuation of 4.5 at the low-energy X-ray spectrum. (a, b) show the ground-truth images. (c, d) show the sinograms at the low-energy and high-energy spectra. The y -axis in (c,d) is along the view dimension. (e, f) and (g, h) show the SIRZ-2 and SIRZ-3 reconstructions respectively. Compared to SIRZ-2, SIRZ-3 reduces both the relative error (equation (14)) and relative RMSE (equation (15)) in Z_e and ρ_e reconstructions. The high relative error associated with SIRZ-2 is also observed by visually comparing (e, f) with (a,b). The noisy ring-like artifacts around the Z_e reconstruction of the copper disk is due to the near zero density of the surrounding air. The unit for ρ_e is electrons \times mol/mm³.

5. RESULTS

Using simulated data, we compared the performance of SIRZ-2 and SIRZ-3 for a wide range of materials and object thicknesses. We chose various materials including pure elements, compounds, and mixtures with effective atomic numbers, Z_e , in the range of 5 – 30 since they are among the most commonly occurring materials that are sensitive to X-rays in our chosen energy range. Our choice of object’s thicknesses was such that the maximum attenuation value for the low-energy DECT spectrum was in the range of 0.5 – 5.5. Outside this attenuation range, it is typically difficult to extract information from X-ray measurements due to the presence of noise. Such a wide selection of materials and attenuations is useful to demonstrate the trends in performance as a function of Z_e and object thicknesses.

We simulated fan-beam X-ray DECT data at 256 different view angles and 256 pixel bins. The low-energy X-ray spectrum is generated using a 100kV bremsstrahlung X-ray source and a 2mm Aluminum filter. The high-energy X-ray spectrum is generated using a 160kV bremsstrahlung X-ray source, a 2mm aluminum filter, and a 2mm copper filter. DECT data is simulated for a circular object that occupies a 224×224 cross-sectional pixel area within the full field-of-view of 256×256 . The source-to-object (SOD) distance and source-to-detector (SDD) distance were chosen to be 500mm and 1000mm respectively. The diameter of the object was adjusted such that we obtained maximum attenuation values of 0.5 to 5.5 in increments of 1.0 for the low-energy spectrum. For each attenuation value, given the atomic composition of the object’s material, we computed the diameter that produces the desired low-energy attenuation along the X-ray path passing through the center of the object. Then, the pixel size for the object was obtained by dividing this diameter by 224 (number of pixels occupied by the object along any direction). We assume a Perkin-Elmer (PE) detector for the detector spectral response. For generating simulated data, we used analytic ray-tracing through geometric solids that is implemented in LTT.⁷ We add 0.1% noise to the measurements in transmission space.

For quantitative comparison of Z_e and ρ_e reconstructions, we utilize two forms of error metrics. The first

Comparison of relative errors (%) in Z_e as defined in equation (14)

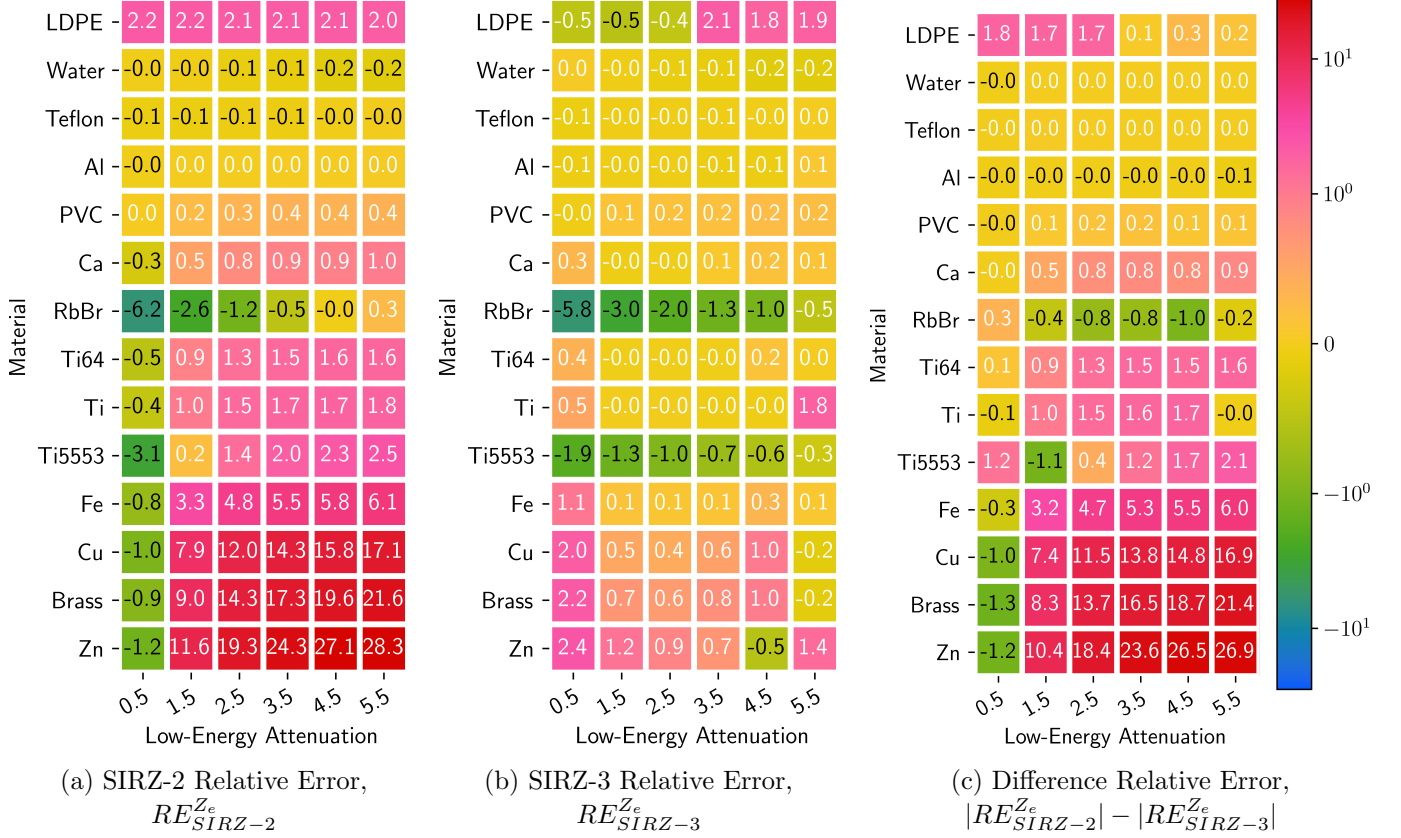


Figure 2. Heat map of the relative error (equation (14)) in reconstruction of Z_e for various materials and maximum low-energy attenuation values, y_L^{max} . (a) and (b) show the relative errors for SIRZ-2 and SIRZ-3 respectively. (c) shows the difference between the absolute values of the SIRZ-2 relative error in (a) and SIRZ-3 relative error in (b). The rows in the heat map are sorted according to the Z_e value. In general, compared to SIRZ-2, the reduction in relative error of Z_e using SIRZ-3 improves with increasing values for Z_e . When the absolute value of the Z_e relative errors with either SIRZ-2 or SIRZ-3 is greater than 1%, SIRZ-3 improves upon SIRZ-2 in 80% of the simulated cases in the heat map.

error metric estimates the bias in the reconstructed values by computing the relative error for either Z_e or ρ_e as,

$$RE_{SIRZ-K}^x = 100 \times \frac{1}{x^{GT}} \left[\left(\frac{1}{|\mathcal{M}|} \sum_{j \in \mathcal{M}} x_j \right) - x^{GT} \right], \quad (14)$$

where $K \in (2, 3)$ is used to denote either SIRZ-2 or SIRZ-3 methods, $x \in (\rho_e, Z_e)$ denotes either ρ_e or Z_e , \mathcal{M} is the set of all pixel indices in the interior of the object that excludes the object boundaries, $|\mathcal{M}|$ is the cardinality (number of elements) of the set \mathcal{M} , and x^{GT} is the ground-truth value for x_j . The second error metric is the relative root mean squared error (RMSE), which is defined as,

$$RMSE_{SIRZ-K}^x = 100 \times \frac{1}{x^{GT}} \sqrt{\frac{1}{|\mathcal{M}|} \sum_{j \in \mathcal{M}} (x_j - x^{GT})^2}, \quad (15)$$

The relative RMSE metric combines both the bias and standard deviation of the difference between the reconstruction and the ground-truth.

In Fig. 1, we compare the performance of SIRZ-2 and SIRZ-3 for a disc of copper (Cu) with a diameter of 4mm and a maximum attenuation of 4.5 at the low-energy spectrum. Fig. 1 (a, b) show the ground-truth (Z_e, ρ_e)

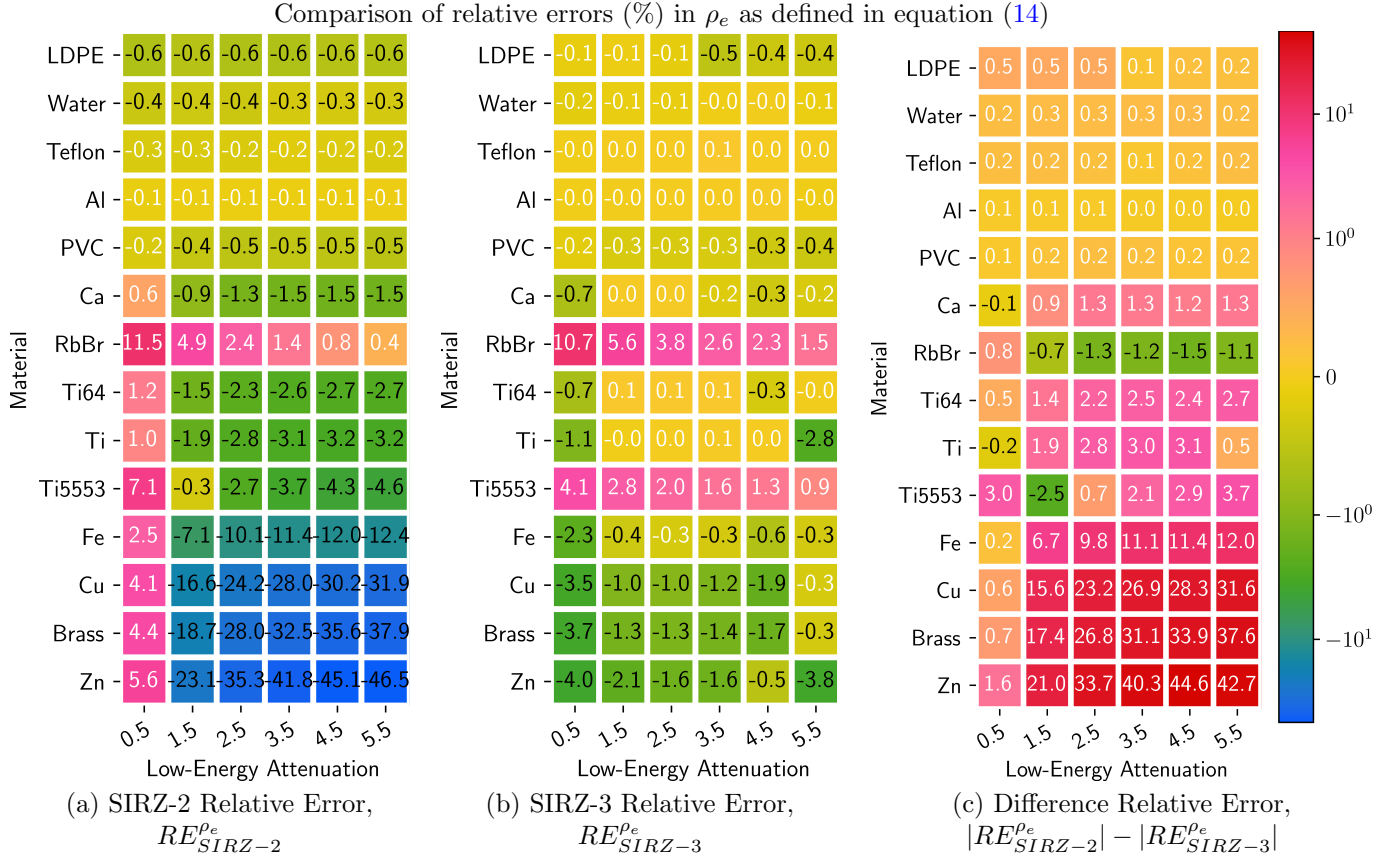


Figure 3. Heat map of the relative error (equation (14)) in reconstruction of ρ_e for various materials and maximum low-energy attenuation values. (a) and (b) show the relative errors (equation (14)) for SIRZ-2 and SIRZ-3 respectively. (c) shows the difference between the absolute values of the SIRZ-2 relative error in (a) and SIRZ-3 relative error in (b). The rows in the heat map are sorted according to the Z_e value. In general, compared to SIRZ-2, the reduction in relative error of ρ_e using SIRZ-3 improves with increasing values for Z_e . When the absolute value of the ρ_e relative errors with either SIRZ-2 or SIRZ-3 is greater than 1%, SIRZ-3 improves upon SIRZ-2 in 87% of the simulated cases in the heat map.

images and Fig. 1 (c, d) show the low-energy and high-energy sinograms. SIRZ-2 and SIRZ-3 reconstructions are shown in Fig. 1 (e, f) and Fig. 1 (g, h) respectively. We can see that both the relative error and the relative RMSE reduces with SIRZ-3 when compared to SIRZ-2. By comparing Fig. 1 (e,f) with Fig. 1 (a,b), we see that SIRZ-2 over estimates the Z_e and under estimates the ρ_e reconstructions. Alternatively, by comparing Fig. 1 (g,h) with Fig. 1 (a,b), we see that SIRZ-3 reduces the bias in Z_e and ρ_e estimates.

In Fig. 2 and 3, we compare the performance of SIRZ-2 and SIRZ-3 using the relative error metric (equation (14)). We compare the relative errors in Z_e and ρ_e for various materials with Z_e in the range of 5 – 30 and maximum low-energy attenuation values, denoted as y_L^{max} , in the range of 0.5 – 5.5. Note that y_L^{max} is the maximum value of low-energy attenuation (modeled using (6)) in the absence of noise. The rows of the heat map are sorted according to ascending values of Z_e . In Fig. 2 and 3, pure element materials are specified by their chemical formula, PVC ($Z_e^{GT} = 14.07$)[‡] denotes polyvinyl chloride, RbBr is 19% RbBr salt solution in water ($Z_e^{GT} = 20.05$, $\rho_e^{GT} = 0.614 \times 10^{-3}$ electrons \times mol/mm³), Ti64 ($Z_e^{GT} = 21.67$) is an alloy of Al (2.8%), Ti (23.9%), and V, Ti5553 ($Z_e^{GT} = 23.73$) is an alloy of Al (3.6%), Ti (32.8%), V (1.9%), Cr (1.1%), and Mo, and brass is an alloy of Cu (1.5%) and Zn.

The reduction in Z_e relative error obtained using SIRZ-3 is quantified in Fig. 2 (c), which shows the difference

[‡] Z_e^{GT} denotes the ground-truth value for Z_e .

between the absolute values of the relative errors using SIRZ-2 (Fig. 2 (a)) and SIRZ-3 (Fig. 2 (b)). A positive value in Fig. 2 (c) indicates that the SIRZ-2 relative error is larger in magnitude than the SIRZ-3 relative error. For LDPE, we observe that the SIRZ-3 absolute[§] relative error is more than 1.5% lower than the SIRZ-2 relative error when $y_L^{max} \leq 2.5$. Beyond LDPE, at low values for Z_e of up to $Z_e = 20$ (calcium), we see that both SIRZ-2 and SIRZ-3 errors are within 1%. Hence, there does not seem to be a benefit to using SIRZ-3 over SIRZ-2 since all errors are below 1%. With RbBr salt solution, we also do not see any apparent advantage of SIRZ-3 over SIRZ-2. For titanium ($Z_e = 22$) and its alloys, we observe a marginal improvement in Z_e performance with SIRZ-3 ($\approx 0\% - 2\%$ reduction in relative error). For materials such as iron (Fe), copper (Cu), brass, and zinc (Zn) with $Z_e \geq 26$, the SIRZ-2 relative errors rise beyond 14% when $y_L^{max} \geq 3.5$. However, we observe that the SIRZ-3 relative error is always less than 2.5% for these materials. From Fig. 2, we observe a trend where the performance of SIRZ-3 over SIRZ-2 improves with increasing values for both y_L^{max} and Z_e when Z_e is greater than ≈ 22 . The Z_e relative errors with SIRZ-3 are almost always within 2.5% (except RbBr) irrespective of the Z_e value. However, the SIRZ-2 relative error increases to more than 25% as the value for Z_e and y_L^{max} is increased. In Fig. 2, SIRZ-3 improves upon SIRZ-2 in 80% of the simulated cases where the absolute value of the Z_e relative errors with either SIRZ-2 or SIRZ-3 is greater than 1%, .

The reduction in ρ_e relative error obtained using SIRZ-3 is quantified in Fig. 3 (c), which shows the difference between the absolute relative errors using SIRZ-2 (Fig. 3 (a)) and SIRZ-3 (Fig. 3 (b)). A positive value in Fig. 3 (c) indicates that the SIRZ-2 relative error is larger in magnitude than the SIRZ-3 relative error. At low values for Z_e of up to PVC, there does not seem to be a benefit to using SIRZ-3 since the relative errors in ρ_e are always under 1%. For calcium, SIRZ-3 reduces the ρ_e relative error by more than 1% when $y_L^{max} \geq 2.5$. SIRZ-3 does not seem to offer any improvements for RbBr salt solution. For Ti and its alloys, the reduction in SIRZ-3 relative error when compared to SIRZ-2 is in the range of 0.5 – 4% when $y_L^{max} \geq 2.5$. For materials such as Fe, Cu, Brass, and Zn with $Z_e \geq 26$, we observe more than 20% reduction in relative error using SIRZ-3 when $y_L^{max} \geq 2.5$. From Fig. 3, we observe a general trend where the ρ_e performance of SIRZ-3 over SIRZ-2 improves with increasing values for y_L^{max} and Z_e when Z_e is greater than ≈ 22 . While the SIRZ-2 relative errors in ρ_e reach very large values of more than 40%, the SIRZ-3 relative errors in ρ_e are almost always under 5% (except RbBr). In Fig. 3, SIRZ-3 improves upon SIRZ-2 in 87% of the simulated cases where the absolute value of the ρ_e relative errors with either SIRZ-2 or SIRZ-3 is greater than 1%.

6. CONCLUSIONS

We presented the SIRZ-3 method for reconstruction of the effective atomic number (Z_e) and electron density (ρ_e) of an object imaged using X-ray dual-energy computed tomography (DECT). We presented a differentiable forward model that expresses the DECT data as a direct analytical function of the unknown (Z_e, ρ_e). SIRZ-3 uses numerical optimization to solve for (Z_e, ρ_e) such that the output of the forward model is close to the measured data. In general, compared to SIRZ-2, the magnitude of performance improvement with SIRZ-3 increases as a function of increasing Z_e . For materials such as iron, copper, brass, and zinc with $Z_e \geq 26$, we show that SIRZ-3 provides more than 10% reduction in Z_e relative error and more than 20% reduction in ρ_e relative error when the maximum low-energy attenuation is greater than 2.5. The large errors for SIRZ-2 at high Z_e is due to approximations made in the dual-energy decomposition and ρ_e/Z_e conversion steps. Due to the absence of these approximations, SIRZ-3 performs better than SIRZ-2. We tested materials with Z_e values in the range of 5 – 30 and low-energy attenuation values in the range of 0.5 – 5.5. During Z_e reconstruction, SIRZ-3 improves upon SIRZ-2 in 80% of our simulated cases where the absolute value of the Z_e relative errors with either SIRZ-2 or SIRZ-3 is greater than 1%. During ρ_e reconstruction, SIRZ-3 improves upon SIRZ-2 in 87% of our simulated cases where the absolute value of the ρ_e relative errors with either SIRZ-2 or SIRZ-3 is greater than 1%.

7. ACKNOWLEDGMENTS

LLNL-CONF-832227. This work was performed under the auspices of the U.S. Department of Energy by Lawrence Livermore National Laboratory under Contract DE-AC52-07NA27344. LDRD 21-FS-013 was used for this project.

[§]Henceforth, relative error refers to the absolute value of the relative error.

REFERENCES

- [1] Martz, H. E., Logan, C. M., Schneberk, D. J., and Shull, P. J., [*X-ray Imaging: fundamentals, industrial techniques and applications*], CRC Press (2016).
- [2] Champley, K. M., Azevedo, S. G., Seetho, I. M., Glenn, S. M., McMichael, L. D., Smith, J. A., Kallman, J. S., Brown, W. D., and Martz, H. E., “Method to extract system-independent material properties from dual-energy x-ray CT,” *IEEE Transactions on Nuclear Science* **66**(3), 674–686 (2019).
- [3] Azevedo, S. G., Martz, H. E., Aufderheide, M. B., Brown, W. D., Champley, K. M., Kallman, J. S., Roberson, G. P., Schneberk, D., Seetho, I. M., and Smith, J. A., “System-independent characterization of materials using dual-energy computed tomography,” *IEEE Transactions on Nuclear Science* **63**(1), 341–350 (2016).
- [4] Liu, D. C. and Nocedal, J., “On the limited memory BFGS method for large scale optimization,” *Mathematical programming* **45**(1), 503–528 (1989).
- [5] Nocedal, J., “Updating quasi-newton matrices with limited storage,” *Mathematics of computation* **35**(151), 773–782 (1980).
- [6] Cullen, D. E., Hubbell, J. H., and Kissel, L., “EPDL97: the evaluated photo data library 97 version,” *Lawrence Livermore National Lab., CA (United States)* (1997).
- [7] Champley, K. M., Willey, T. M., Kim, H., Bond, K., Glenn, S. M., Smith, J. A., Kallman, J. S., Brown, W. D., Seetho, I. M., Keene, L., Azevedo, S. G., McMichael, L. D., Overturf, G., and Martz, H. E., “Livermore tomography tools: Accurate, fast, and flexible software for tomographic science,” *NDT & E International* **126**, 102595 (2022).
- [8] Shi, H.-J. M. and Mudigere, D., “PyTorch-LBFGS: A PyTorch implementation of L-BFGS,” <https://github.com/hjmshi/PyTorch-LBFGS> .